ISPRS Journal of Photogrammetry and Remote Sensing 165 (2020) 1–15

Contents lists available at ScienceDirect

ISPRS Journal of Photogrammetry and Remote Sensing

journal homepage: www.elsevier.com/locate/isprsjprs

Complete and accurate data correction for seamless mosaicking of airborne hyperspectral images: A case study at a mining site in Inner Mongolia, China

Kun Tan[b,a,*], Chao Niu[a,b], Xiuping Jia[c], Depin Ou[a], Yu Chen[a], Shaogang Lei[a,*]

[a] NASG Key Laboratory of Land Environment and Disaster Monitoring, China University of Mining and Technology, Xuzhou 221116, China
[b] Key Laboratory of Geographic Information Science (Ministry of Education), East China Normal University, Shanghai 200241, China
[c] School of Engineering and Information Technology, The University of New South Wales, Canberra, ACT 2600, Australia

ARTICLE INFO

Keywords:
Airborne hyperspectral
Radiation correction
BRDF
Radiation attenuation

ABSTRACT

Airborne hyperspectral remote sensing is an important application in the ecological monitoring of the environment in mining areas, and accurate preprocessing of the original images is the key to quantitative information retrieval. The original image data need radiation correction to acquire surface reflectance data. Due to the impact of the field angle, incidental radiance, and the bidirectional reflectance distribution function (BRDF), there can be a brightness gradient between adjacent strips, which leads to radiance difference and obvious chromatic aberration of the mosaicked images. We propose a novel data correction method for seamless mosaicking of airborne hyperspectral images. Firstly, visible and near-infrared (VNIR) and shortwave infrared (SWIR) sensors are calibrated in the laboratory, and the radiation calibration model of the sensor is established by an integrating-sphere system. A correction function is then established by combining the BRDF effect and the radiation attenuation coefficients. We also normalize the exposure time, sun altitude angle, and sensor altitude angle according to the flight strip. The results showed that this method is able to eliminate the signal distortion, allowing the seamless mosaicking of 37 strip images which were taken in different date and conditions in the study area. After the atmospheric correction of the imagery was completed, the accuracy of the preprocessing results was evaluated by field-measured ASD spectroradiometer data. The coefficient of determination R^2 of the results for the reflectance was greater than 0.9. The experiments show that the proposed method has a good performance in radiation accuracy, and can provide high-quality hyperspectral data for the follow-up application of the ecological monitoring of a mining area.

1. Introduction

For the qualitative and quantitative environmental analysis using airborne hyperspectral remote sensing data, high-precision data acquisition and processing are the key to success. The reliability and validity of images are affected by several factors, including the atmospheric effect, variations in observation angle, and instrument limitation, which need to be corrected completely and accurately. Satellite hyperspectral data, such as from EO-1 Hyperion, have spatial resolution of 30 m, in order to have high spectral resolution of 10 nm. To have better spatial resolution, spectral resolution is often compromised, for example, the image data from WorldView. On the other hand, airborne hyperspectral remote sensing data can have relatively high spatial resolution and high spectral resolutions as well, and are suitable for detailed land cover classification (Tan et al., 2015; Wang et al., 2019), the prediction of soil heavy metal content (Tan et al., 2020; Wu et al., 2011), and the inversion of vegetation parameters (Darvishzadeh et al., 2008; Wang et al., 2018). In open-pit mining areas, studies have been conducted on the pollution of metallic minerals in soils (Choe et al., 2008) and rivers (Riaza et al., 2012) caused by mining activities, and the monitoring of revegetation in mining areas (Lévesque and Staenz, 2004). Such data can provide a reliable scientific background for environmental decision makers in mining areas. As all of the above studies rely on data calibration and spectral reconstruction, the preprocessing of the hyperspectral data is particularly important.

In terms of spectral calibration, Cocks et al. (1998) completed spectral correction of HyMap hyperspectral imager data using a monochromator. In-flight absolute calibration and the integrating-sphere system are common radiometric calibration methods (Chen

* Corresponding authors at: Key Laboratory of Geographic Information Science (Ministry of Education), East China Normal University, Shanghai 200241, China (Kun Tan).
E-mail addresses: tankuncu@gmail.com (K. Tan), lsgang@126.com (S. Lei).

https://doi.org/10.1016/j.isprsjprs.2020.04.022
Received 28 October 2019; Received in revised form 30 April 2020; Accepted 30 April 2020
Available online 16 May 2020

et al., 2013; Gege et al., 2009). After radiometric calibration, the atmospheric correction of radiance data needs to be undertaken to obtain the real surface reflectance. The most common atmospheric correction methods are based on radiative transfer models such as moderate resolution atmospheric transmission (MODTRAN) and Second Simulation of a Satellite Signal in the Solar Spectrum (6S) (Berk et al., 1987; Vermote et al., 1997). In addition, a supervised vicarious calibration method without radiometric calibration has also provided a good spectral accuracy for airborne hyperspectral images, especially for sensors with questionable or uncertain laboratory-determined radiometric parameters (Brook and Ben-Dor, 2015; Brook and Dor, 2011; Pan et al., 2018). However, compared with laboratory calibration, the real-time acquisition of ground spectral data and the determination of the observation geometry are the limitations of this approach.

After completing atmospheric correction, it is necessary to mosaic the single strips to obtain a multi-strip image. Most processing of airborne hyperspectral images ends here, without considering radiation correction across strips, and light and shade differences and discontinuities between the strips appear in the mosaicked image. These differences and discontinuities make it difficult to maintain the spatial uniformity of the image radiance and destroy the integrity of the image (Collings et al., 2010; Jensen et al., 2017). This systematic variation in intensity is mainly caused by the bidirectional reflectance distribution function (BRDF) effect, which is usually used to describe the anisotropy of rough surfaces (Lucht et al., 2000; Schaepman-Strub et al., 2006). The anisotropic reflection characteristics of the BRDF effect arise from the physical structure of the measured surface, where the different surfaces acquired in the image have different anisotropic scattering characteristics, so the BRDF of each surface has different effects on the observed albedo (Jensen et al., 2017). Focusing on the correction of hyperspectral imagery, the widely used technique for BRDF correction is to fit the model to the image data, and then eliminate the differences and discontinuities. However, due to the dependence of reflectance on the varying views, incident light angles, reflect angles, and so on (Collings et al., 2010; Rogge et al., 2012), it is necessary to build a model and apply angle normalization to eliminate the influence of the observation geometry.

The correction model can be physical, empirical, or semi-empirical. A physical model, such as the radiative transfer model or the geometric-optical model, is based on the physical process of the interaction between incident light and the surface, and establishes the relationship between the bidirectional reflectance of the surface and the surface parameters. This approach is commonly used in the study of vegetation canopy reflectance (Li and Strahler, 1992). In the field of hyperspectral imaging, empirical and semi-empirical models are more widely used. An empirical model mainly considers the statistical characteristics of the image, establishes the polynomials, and fits the view angle dependence on the mean radiance brightness along the viewing direction by the least-squares method, so that the compensation coefficients can correct the off-nadir reflectance with nadir values (Kennedy et al., 1998; Rautiainen et al., 2008). In addition, empirical models, such as the Lommel-Seeliger model, have been used for photometric correction on the lunar surface (Wu et al., 2013). The semi-empirical models consider the mechanism of illumination and reflection on the surface objects, and construct a multi-parameter fitting model or a semi-empirical kernel-based model to complete the correction. Because of the physical significance and multi-parameter modeling, the semi-empirical approach is widely used in hyperspectral image processing. Collings et al. (2010) conducted BRDF correction for each strip of a HyMap image mosaic based on Ross-Li kernels. Colgan et al. (2012) used an improved Ross-Li kernel to complete BRDF correction of aerial hyperspectral images and eliminate the line artifacts in species probability maps. The Hapke model with particle shape and roughness was developed for radiation correction across strips and seamless mosaicking of hyperspectral images (Hapke, 2012; Yu et al., 2017). The above methods are based on the assumption of radiance uniformity, and are generally applicable in conditions having flat terrain and minimal true land-cover change. In the areas with mountainous terrain or complex terrain types, topographic relief and land-cover types are required to consider to achieve good results (Jensen et al., 2017; Li et al., 2012). Schläpfer et al. (2014) developed a continuous BRDF cover index function for different surface cover change, from water to soil and vegetation. For the supervised vicarious calibration of hyperspectral sensors, (Brook et al., 2018) developed a correction method using the BRDF correction coefficient measured on the ground targets with different illumination zenith and azimuth angles..

Radiation attenuation caused by the difference of the radiation transmission path is also a factor of distortion. The study of radiation path difference considers the effect of sensor height and altitude on the apparent radiance of a target on the Earth's surface (Horvath et al., 1970; Van Stokkom and Guzzi, 1984). In addition to the sensor height and altitude, the inconsistency of the radiation path caused by the flight attitude and sensor field of view angle also affects the radiation. The precise estimation of radiation attenuation often requires a good knowledge of aerosol optical properties to establish an attenuation model to eliminate radiation loss. However, this information is difficult to measure and generally unavailable (Polo et al., 2016). For an imaging spectrometer, the statistical model can be established from the acquired image data, and the corresponding radiation attenuation can be obtained by the radiation path difference and the assumption of brightness uniformity (Patterson et al., 1977; Tian et al., 2016).

In this paper, we focus on cross strips radiation distortion caused by radiation attenuation and the BRDF effect, and we introduce the radiation attenuation coefficient and BRDF coefficient on the basis of the radiance uniformity assumption. In this paper, differing from the previous correction models, we consider the influence of flight attitude on the radiation path, and we use position and orientation system (POS) data to analyze the attitude of the sensor. We then calculate the radiation path difference corresponding to the different angles of view. Exposure time correction of the sensor is also completed. Considering the influence of the sensor angle, solar zenith angle, and sensor zenith angle on the directional reflection of ground objects, the correction function for edge radiation distortion is constructed. The relevant angle and plane references used in this paper are shown in Fig. 1.

Differing from most other studies (Kennedy et al., 1998; Schläpfer et al., 2014; Yu et al., 2017), more difficulties were encountered in this study including:

1) Due to the influence of the solar altitude angle and the limitation of the image digitization, different exposure times were set at different flight times and the exposure time needed to be corrected.
2) The flight experiment was conducted for a long time span. It lasted three days, and the total flight time was about 7.6 h. A large number of flight strips (37) were generated. The raw data volume was over 2 TB.
3) The longest single flight time was longer than 4 h, so the solar altitude angle varied greatly, which brought new challenges to the correction.

In this study, we propose a radiance correction method which considers the BRDF and radiation attenuation for seamless mosaicking of airborne hyperspectral images. The exposure time correction term and the Lommel-Seeliger factor were added to the correction model. In addition, the sensor attitude data were used to correct the radiation transmission path error. The study is valuable in improving the quality of the obtained airborne hyperspectral images, which is important for various qualitative and quantitative analysis. Accordingly, this paper will be the first to describe a full correction method to address a number of error factors. A sensitivity test is used to correct the exposure time. The radiation distortion is achieved by establishing a correction function which considers the BRDF effect and radiation attenuation caused by sensor attitude, for a seamless mosaic of strips recorded over a long

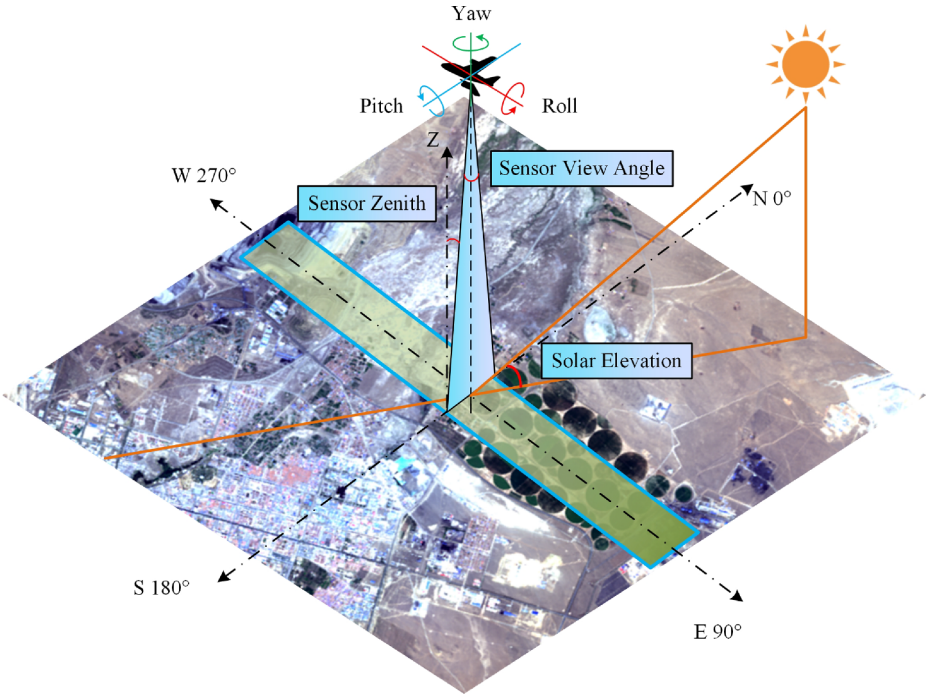

Fig. 1. The relevant angle and plane references to the actual flight situation. The solar elevation is the angle between the horizon plane and the sun's rays. The sensor zenith angle is the angle between the zenith and the sensor's observation direction. The sensor view angle is the angular extent of a given sensor.

time span. The mosaicked results and radiance values before and after correction are examined, and the correction accuracy is evaluated using the ground field spectroradiometer data collected.

2. Study area and data overview

2.1. Study area

The city of Xilinhot is located in Xilingol League, the central part of the Inner Mongolia Autonomous Region. The latitude of the city is 43° 02′ to 44° 52′ N, and the longitude is 115° 18′ to 117° 06′ E. The landscape is mainly a high plain area, with an average elevation of about 1000 m. The terrain of the study area is relatively gentle, and the main land cover type is the bare earth. The area holds abundant mineral resources, including oil, coal, germanium, and molybdenum. The proven reserves of coal are 33.7 billion tons, of which 22.4 billion tons are located in the Shengli coalfield, which is the largest lignite coalfield in China. The open-pit mining area is located in the northern part of the city of Xilinhot. The mine belongs to the Shenhua Beidian Shengli Energy Co., Ltd., the Inner Mongolia Datang International Xilinhot Mining Co., Ltd., and the Xilingole Wulantuga Coal Co., Ltd. The Shenhua-Shengli mining area was considered as the key research area in this study, as shown in Fig. 2. The flight area covered about 500 square kilometers, totaling 37 strips.

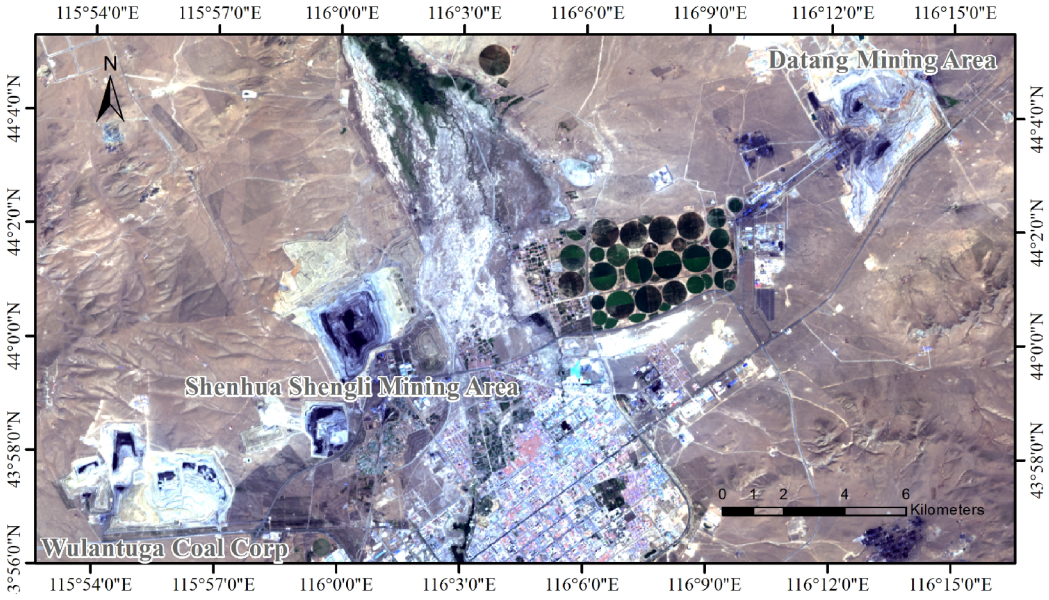

Fig. 2. Geographic location of the study area. Acquired by the Landsat8 OLI and RGB color composition using band 4, band 3, band 2.

Table 1
Hyperspectral imager parameters.

Parameter	Headwall A-Series	HySpex SWIR-384
Spectral range/nm	380–1000	950–2550
Spectral resolution/nm	2.5	5.45
Bands	837	288
Samples	1004	384
Frame frequency/Hz	90	400
FOV/°	34	16
Digitization/bit	12	16
Sensor weight/kg	2.8	5.7
Sensor power/W	6.6	30

2.2. Sensor parameters and flight design

In this flight experiment, two hyperspectral imagers—a Headwall A-Series VNIR hyperspectral imager and a HySpex SWIR-384 hyperspectral imager—measures the solar spectral domain from the visible and near infrared (VNIR) to the short wave infrared (SWIR). The Headwall A-Series VNIR hyperspectral imager is manufactured by Headwall Photonics, Inc., USA. The spectral range is 380–1000 nm. This hyperspectral imager provides high spatial resolution and hyperspectral resolution image data for the on-line monitoring of production processes and remote sensing applications. The HySpex SWIR-384 is developed by the Norwegian NEO company. The spectral range is 950–2550 nm. It has a high signal-to-noise ratio and can obtain high dynamic range and high-quality hyperspectral image data. This hyperspectral imager is widely used in laboratories, aerospace applications, and other fields. The specific parameters of the two sensors are listed in Table 1, and the flight design is shown in Table 2. The SPAN-CPT one-piece closed-loop fiber optic integrated navigation system provides the high-precision position and orientation data. It is developed by NovAtel company, and the position and orientation are measured with a NovAtel SPAN-CPT Global Navigation Satellite System (GNSS)/INS, and its performance is listed in Table 3.

Table 2
Flight plan.

Flight parameters	
Image width	HeadWall: 1222.92 m; HySpex:555.63 m
Sidelap	HeadWall: 68%; HySpex: 30%
Altitude	2000 m
Strips	37
Average length of each strip	About 31.8 km
Direction	east–west
Flight area	about 451.9175 km^2
Speed	300 km/h
Time interval	10:30am-2:30 pm
Imager acquisition time	3.922 h
Take-off and turn time	3.7 h
Total flight time	7.622 h

3. Methodology

In most image preprocessing, radiation correction across strips is not a necessary step when a single strip image is analyzed, but it does play an important role in eliminating radiation distortion, acquiring accurate radiance information, and seamless mosaicking of multiple strips. The mismatch between strips is due to the BRDF effect and radiation distortion. The radiation correction method proposed in this paper corrects the BRDF effect and radiation transmission path error caused by the change of the sensor's attitude, and introduces an exposure time correction term and the Lommel-Seeliger factor. The correction coefficients are calculated to normalize the angle of view and solar altitude, and eliminate the exposure time differences and radiation attenuation.

3.1. Sensor laboratory testing and calibration

3.1.1. Sensor laboratory testing

Sensor laboratory testing is the basis of precise quantitative application. Before the data acquisition, the laboratory tests and calibration of the sensors need to be carried out. The test contents included wavelength calibration, sensitivity testing, spectral distortion testing, and so on. The wavelength calibration involved the use of a monochromator to calibrate the central wavelength and bandwidth of each band (Cocks et al., 1998), which is the premise and guarantee of radiation calibration. By analyzing and comparing the output wavelength of the monochromator with the corresponding band of the hyperspectral imager, accurate calibration of the wavelength was completed by linear fitting. The sensitivity contrast test was completed by setting the integrating sphere power and integrating time and comparing the spectral curve of the sensor.

3.1.2. The exposure time sensitivity test and radiometric calibration

In order to verify the effect of exposure time on DN values, we used the integrating sphere system to determine the functional relationship between DN value and exposure time by setting different exposure conditions in the laboratory. The integrating-sphere system can provide a standard radiation surface source with high accuracy and stability. It includes an integral sphere, a standard source, and a controller, which is used to set the output power and integration time. The schematic diagram of the system is shown in Fig. 3. The exposure time sensitivity test was completed by setting different sensor exposure time under the same integration power.

In addition, the obtained integral sphere data can be used for radiometric calibration. The radiometric calibration of the spectrometer is completed by fitting the radiance value with the digital number (DN) output data of the imaging spectrometer with the least-squares method. The calibration formula is as follows:

$$L_z = a_z DN_z + b_z, \quad (1)$$

where L_i is the radiation brightness value in band z, a_z is the gain coefficient in band z, b_z is the offset value in band z, and DN_z is the

Table 3
Integrated navigation systems performance.

Outage duration	Positioning mode	Position accuracy (m) RMS		Velocity accuracy (m) RMS		Attitude accuracy (degrees) RMS		
		Horizontal	Vertical	Horizontal	Vertical	Roll	Pitch	Heading
0 s	Single Point	1.0	0.60	0.02	0.01	0.02	0.02	0.06
	Post-processing	0.01	0.02	0.015	0.01	0.008	0.008	0.035
10 s	Single Point	1.2	0.75	0.05	0.025	0.03	0.03	0.08
	Post-processing	0.02	0.02	0.015	0.01	0.008	0.008	0.035
60 s	Single Point	7.0	2.6	0.26	0.08	0.045	0.045	0.1
	Post-processing	0.23	0.11	0.02	0.012	0.013	0.013	0.038

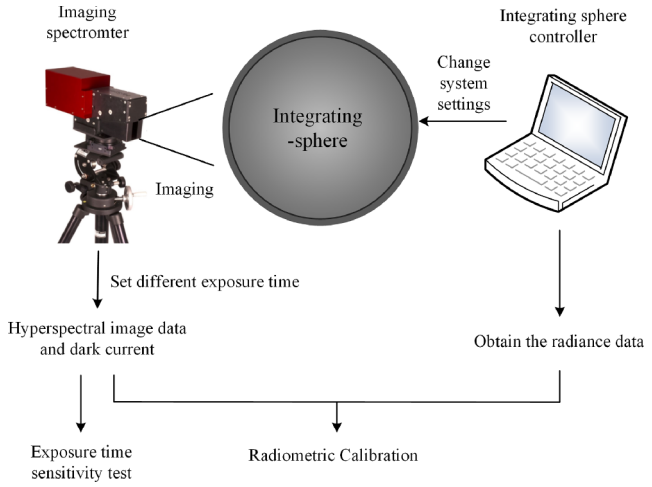

Fig. 3. The schematic diagram of integrating-sphere system.

output brightness value in band z.

3.1.3. Exposure time correction

In the process of hyperspectral image acquisition, due to the influence of the illumination intensity and the image digitization, an excessive exposure time will lead to over-saturation, which means that the DN value reaches the upper limit of the imager storage and it cannot distinguish the spectral characteristics of the ground objects. Due to the large time span and unstable flight control, different exposure times may be used in different strips, which thus needed to be corrected according to the exposure time.

The DN value obtained by the sensor is positively correlated with the exposure time, and the specific functional relationship can be obtained by fitting the exposure time and DN value tested in the laboratory. Here we use function $E(t)$ to express the corresponding relationship between DN value and exposure time. The calculation formula for the exposure time correction coefficient e is as follows:

$$e = \frac{E(\bar{t})}{E(t)}, \tag{2}$$

where $\bar{t}$ is the unified exposure time, which is set according to the actual experimental conditions, and t is the exposure time of this strip.

After the exposure time sensitivity test, seven groups of average DN values were obtained with the exposure times ranging from 5 ms to 35 ms, where the DN value was the average value calculated by all bands obtained by the HeadWall VNIR imager. Fig. 4 shows the relationship between the exposure time and DN value. It can be seen that the DN value is proportional to the exposure time, so the images acquired by sensors with different exposure times can be corrected to the same exposure time by the corresponding ratio to eliminate the difference in the image radiance caused by the exposure time. The calculation formula for the exposure time correction coefficient e can be further simplified as follows:

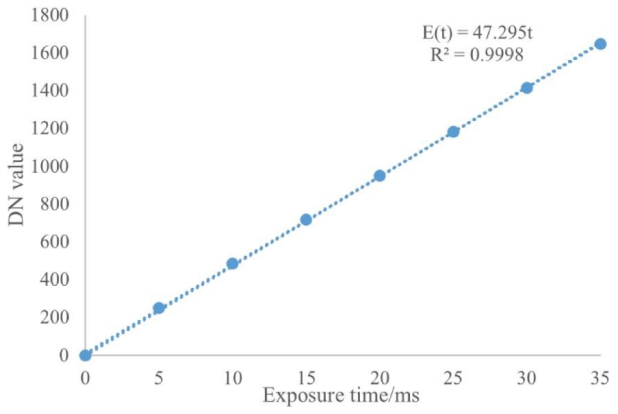

Fig. 4. Fitting line of exposure time versus DN value.

$$e = \frac{\bar{t}}{t}, \tag{3}$$

here we set the normalized exposure time $\bar{t}$ to 13.72 s according to the actual flight situation, as shown in Fig. 5.

3.2. Radiation transmission path correction

The change of sensor attitude causes displacement between the scanning center point and the nadir, which changes the radiation transmission path and leads to radiation attenuation. This error is mainly caused by the change of the pitch and roll angle of the aircraft. In the following, we discuss the accuracy of position and attitude and the effects of several different attitude changes on the radiation transmission path.

3.2.1. Position and attitude system and error analysis

The accuracy of position and attitude is critical in calculating the radiation transmission path difference. When the aircraft was in air, the position and attitude data of the sensor were obtained by the inertial navigation system (INS) in real time. In this study, we calibrated the system error and evaluated the position and attitude data accuracy by the direct geo-referencing method.

First, the post-processing and system error correction were carried out by using the Inertial Explorer software to obtain the high-precision position and attitude data of the aircraft. Then, the exterior orientation element was solved, and positioning accuracy was calculated according to the deviation from the ground control point. Table 4 shows error analysis for 10 control points measured by Real-Time Kinematic (RTK). The Root Mean Square Error (RMSE) of plane is 1.844 m, and the RMSE of height is 0.894 m. The position and attitude data accuracy meets the experimental requirements.

3.2.2. Pitch angle correction

The change of the radiation transmission path caused by the pitch angle of the aircraft is illustrated as follows. It can be seen from Fig. 5 that the effect of the pitch up or down is consistent. The larger the pitch angle, the longer the radiation transmission path. The radiation path difference caused by the pitch angle is as follows, where H is the altitude and θ_p is the pitch angle.

$$\Delta H_p = H\left(\frac{1}{\cos\theta_p} - 1\right). \tag{4}$$

Table 4
Position and attitude data error statistics.

Point number	Plane error (m)			Height error (m)
	Dx	*Dy*	*Dxy*	*Dz*
1	0.77	−0.35	0.845	0.86
2	3.03	0.58	3.085	0.76
3	0.75	0.75	1.06	1.21
4	−0.73	1.30	1.49	1.04
5	−1.47	−0.70	1.628	0.31
6	0.92	−0.07	0.922	0.43
7	−0.5	0.94	1.064	0.17
8	−0.42	1.69	1.741	1.56
9	−1.8	2.54	3.113	0.98
10	1.25	1.23	1.753	0.73
RMSE	1.38	1.22	1.844	0.894

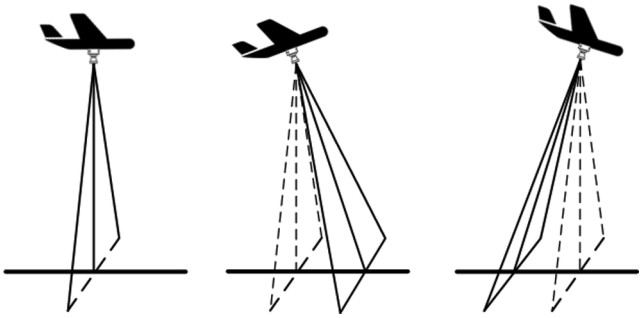

Fig. 5. Pitch angle change in flight.

3.2.3. Roll angle correction

The change of the radiation transmission path caused by the roll angle is related to the field of view angle of the sensor. Taking forward clockwise rolling as an example, it can be seen from Fig. 6 that when the angle of roll increases from 0^0 to half of the field of view, the angle of view at the right edge of the scanning center is perpendicular to the ground, and the radiation transmission path is the smallest. When the roll angle continues to increase, the radiation transmission path increases gradually. Therefore, considering the change of the sensor's angle of view, the change of the radiation path caused by the roll angle is as follows:

$$\Delta H_r = H\left(\frac{1}{\cos(\theta_r + \theta_i)} - 1\right), \tag{5}$$

where H is the altitude; θ_r is the roll angle; and θ_i is the sensor's angle of view. The Headwall A-Series sensor's field of view ranges from -17° to 17°. The HySpex SWIR-384 sensor's field of view ranges from -8° to 8°. By synthesizing the roll angle, the final radiation path difference ΔH is obtained as follows:

$$\Delta H = H\left(\frac{1}{\cos(\theta_r + \theta_i)} + \frac{1}{\cos\theta_p} - 2\right). \tag{6}$$

3.2.4. Sensor zenith angle

The influence of the pitch angle and roll angle should be taken into account when calculating the sensor zenith angle. The sensor zenith angle is shown in Fig. 7, and the formula for calculating the zenith angle of the sensor is as follows, where θ_p is the pitch angle and θ_r is the roll angle.

$$\theta_z = \arccos(\cos\theta_r \cos\theta_p). \tag{7}$$

3.2.5. Radiation attenuation coefficient

The radiation attenuation coefficient is usually expressed in the differential form of Bougner's theorem (Baldocchi et al., 1984):

$$dL(\lambda) = -\mu(\lambda)L(\lambda)dh, \tag{8}$$

where λ is the wavelength, $dL(\lambda)$ is the unit attenuation, $L(\lambda)$ is the radiation intensity, $\mu(\lambda)$ is the radiation attenuation coefficient, and dh is the atmospheric thickness. Some studies have solved the radiation

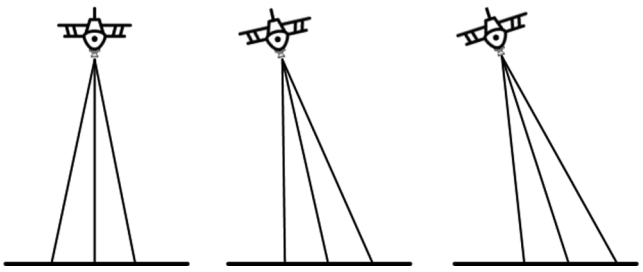

Fig. 6. Roll angle change in flight.

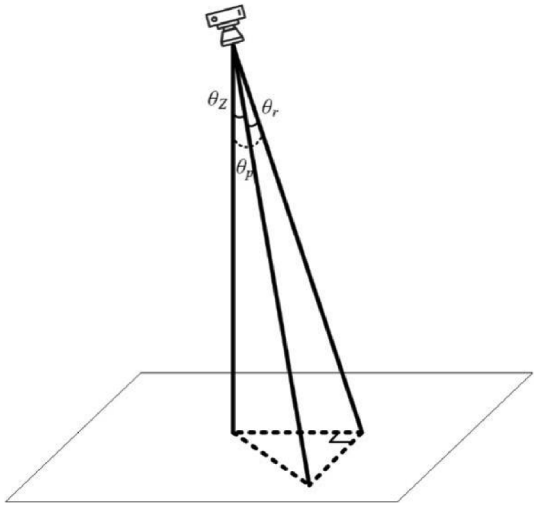

Fig. 7. Sensor zenith angle.

attenuation coefficient through the assumption of radiance uniformity (Tian et al., 2016), which means that the column mean of the radiance is approximated in a straight line without radiation distortion. However, this assumption is affected by the distribution of the land cover and topographic fluctuations, and the BRDF effect also needs to be eliminated. In this paper, the radiation path difference caused by the sensor attitude and angle of view is calculated, and the empirical model is constructed as a factor of BRDF correction in the next step.

According to the Bougner-Lambert transmission law (Patterson et al., 1977), the radiance after radiation attenuation from the view angle of θ_i is as follows:

$$L_{\theta_i}(\lambda) = L_s(\lambda)e^{-\int_0^{H+\Delta H_{\theta_i}} \mu(\lambda)dh}, \tag{9}$$

where λ is the wavelength, L_s (λ) is the radiance of the ground object, H is the flight altitude, and $\Delta H_{\theta i}$ is the radiation path difference calculated by Eq. (6). Considering Eq. (8), it can be simplified as follows:

$$L_{\theta_i}(\lambda) = L_s(\lambda)e^{\frac{(H+\Delta H_{\theta_i})dL(\lambda)}{L(\lambda)}}. \tag{10}$$

It is difficult to quantify $dL(\lambda)$ under the influence of atmospheric conditions, so we introduce the attenuation coefficient term by considering the radiation path difference. The radiation coefficient term $\frac{(H+\Delta H_{\theta_i})dL(\lambda)}{L(\lambda)}$ can be further simplified. Finally, the radiance after radiation attenuation is obtained as follows:

$$L_{\theta_i}(\lambda) = \left(1 - e^{g(\theta_i)}\right) L_s(\lambda), \tag{11}$$

where $e^{g(\theta_i)}$ is the attenuation coefficient term for BRDF correction in the next step, and $g(\theta_i)$ is the fitting function about the sensor's angle of view and the radiation path difference. There is no need to take the accurate value of fitting parameters, but to determine the fitting equation form, so as to participate the BRDF correction coefficient in the next step.

In order to determine the fitting equation form of this experiment, five hundred lines of POS data were selected to construct the radiation path difference from different angles of view mentioned in Eq. (6), and the mean value was calculated to draw the fitting line in Fig. 8. The result was a quadratic linear regression equation and the $g(\theta_i)$ can be expressed as follows:

$$e^{g(\theta_i)} = e^{b_0 + b_1\theta_i + b_2\theta_i^2}, \tag{12}$$

where b_0, b_1, b_2 are the least-squares fitting coefficients.

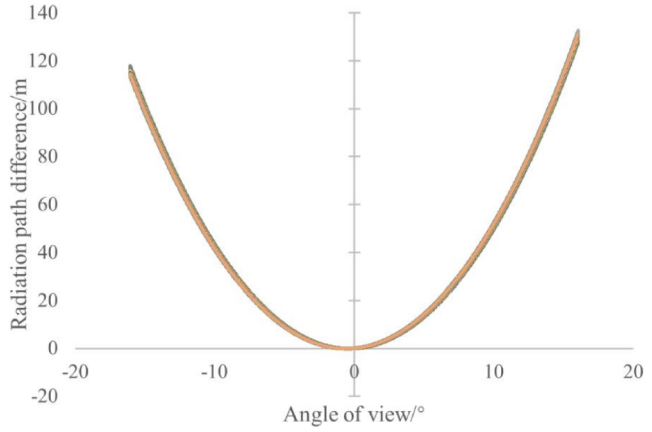

Fig. 8. Radiation path difference curve.

3.3. BRDF coefficient correction

The BRDF coefficient correction considers the radiation distortion caused by the change of the sensor angle view and the transmission path difference mentioned in Section 3.2. According to the radiance uniformity assumption, we use the average radiance of the different views to establish a univariate quartic empirical model as follows:

$$f(\theta_i) = a_0 + a_1\theta_i + a_2\theta_i^2 + a_3\theta_i^3 + a_4\theta_i^4 + e^{g(\theta_i)}, \quad (13)$$

where θ_i is the angle of view; $f(\theta_i)$ is the average radiance value at the angle of θ_i; and a_0, a_1, a_2, a_3, and a_4 are the least-squares fitting coefficients. Different from the quadratic fitting established in previous studies (Kennedy et al., 1998; Wu et al., 2013; Yu et al., 2017), a quartic fitting model is established for BRDF correction of hyperspectral images. In addition, most of the empirical and semi-empirical methods for BRDF correction of hyperspectral images ignore the image radiation attenuation. Here we consider the radiation attenuation caused by the sensor attitude and introduce the attenuation coefficient term in Eq. (12).

In order to correct the angle of view to normalization angle 0°, the BRDF correction coefficient c from the different angle of view is:

$$c = \frac{a_0 + e^{g(\theta_{i=0})}}{f(\theta_i)} \quad (14)$$

The BRDF correction coefficient c from the different angle of view mentioned in Eq. (12) can be further rewritten as follows:

$$c = \frac{a_0 + e^{b_0}}{f(\theta_i)}. \quad (15)$$

In addition to correcting the influence of the sensor's angle of view, normalization of the solar zenith angle and the sensor zenith angle is also needed. Considering the description of the directional reflection characteristics of ground objects in the Hapke model and Lommel-Seeliger function (Hapke, 2002; Wu et al., 2013), the Lommel-Seeliger factor $\frac{\mu_s}{\mu_s+\mu_z}$ is introduced as follows:

$$\frac{\mu_s}{\mu_s + \mu_z} = \frac{\cos\theta_s}{\cos\theta_s + \cos\theta_z}, \quad (16)$$

where θ_s is the solar zenith angle and θ_z is the sensor zenith angle.

Considering all the factors that cause radiation attenuation, we finally obtain the revised radiation attenuation correction function as follows:

$$P_z(\theta_i) = ec_z L_z(\theta_i) \frac{\cos\theta_s}{\cos\theta_s + \cos\theta_z} \frac{\cos\bar{\theta}_s + \cos\bar{\theta}_z}{\cos\bar{\theta}_s}, \quad (17)$$

where θ_i is the angle of view, $P_z(\theta_i)$ is the corrected radiance in the zth band, e is the exposure time correction coefficient, and c_z is the BRDF correction coefficient in the zth band. $L_z(\theta_i)$ is the original radiance. θ_s and θ_z are the solar zenith angle and sensor zenith angle, obtained using POS data to obtain the mean value by line. $\bar{\theta}_s$ is the normalized solar zenith angle, which is set to 40°, as the average sun zenith angle of all the strips. $\bar{\theta}_z$ is the normalized solar zenith angle, which is set to 0°.

Table 5
The parameters used in the MODTRAN4 atmospheric correction model.

Parameters	
Atmospheric Model	Mid-Latitude Summer
Solar Spectral Irradiance Resolution (cm^{-1})	5
Boundary Temperature (K)	283.15
CO_2 Mixing Ratio (ppmv)	380
H_2O Column Amount (gm/cm^2)	1.3
O_3 Column Amount (gm/cm^2)	0.0015

3.4. Ground spectra data collection and accuracy assessment

After radiation correction, we used the MODTRAN model for atmospheric correction. The parameters used in the process are listed in Table 5. The Mid-Latitude Summer atmospheric model was selected according to the flight date and position of longitude and latitude. The meteorological parameters were obtained by the local environmental monitoring station. Since atmospheric correction methods are not the focus of this study, this section focuses on the ground spectra data collection and accuracy assessment of the processed data.

At the same time as the flight, typical ground objects' spectra (including vegetation and soil) and locations were collected synchronously, strip by strip. An ASD FieldSpec 4 field spectroradiometer was used to collect the spectra of typical ground objects. Five sets of spectral data were obtained, and the average value was taken as the reflection spectrum of the object. The ASD field spectroradiometer spectra were used to compare and validate the reflectance data after atmospheric calibration. The accuracy was evaluated by the commonly used evaluation indexes: determination coefficient R^2 and RMSE. In addition, the spectral angle (SA) was selected to evaluate the similarity between the corrected image spectrum and ground object spectrum.

$$\cos\alpha = \frac{\vec{\mathbf{t}} \cdot \vec{\mathbf{r}}}{\|\vec{\mathbf{t}}\| \times \|\vec{\mathbf{r}}\|} = \frac{\sum_{i=1}^{n} t_i r_i}{\sqrt{\sum_{i=1}^{n} t_i^2} \times \sqrt{\sum_{i=1}^{n} r_i^2}}, \quad (18)$$

where n is the number of the band, $\vec{\mathbf{t}} = (t_1, t_2 \ldots, t_n)$ is the corrected image spectrum, $\vec{\mathbf{r}} = (r_1, r_2 \ldots, r_n)$ is the ground object spectrum. α is the spectral angle with a range of 0–90°. The lower the α value, the higher the similarity. Spectral angle less than 0.3 rad (17.2°) can be considered high degree of similarity.

4. Results and assessment

4.1. Sensor laboratory testing results

The results of the wavelength calibration are shown in Fig. 9, where the determination coefficient R^2 of the Headwall A-Series sensor and the HySpex SWIR-384 sensor after wavelength calibration were 0.99999 and 0.99998, respectively. The experiment showed the good fitting effect with a high coefficient of determination. After wavelength calibration, the exact central wavelength and bandwidth of each band were obtained for radiation calibration. The results of sensitivity testing are shown in Fig. 10. Through the comparative experiments of different integral power, it was found that the Headwall A-Series sensor and the HySpex SWIR-384 sensor can react accurately to integrating spheres of different power, and the sensitivity of the imagers met the requirements.

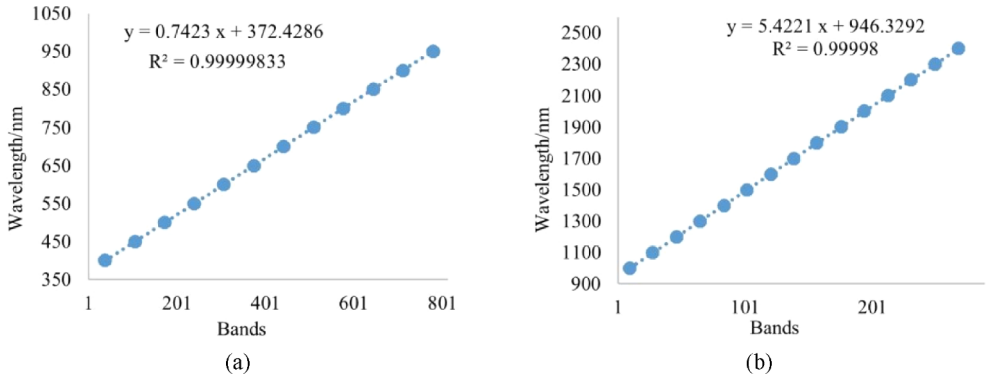

Fig. 9. Wavelength calibration result for (a) the Headwall A-Series sensor and (b) the HySpex SWIR-384 sensor.

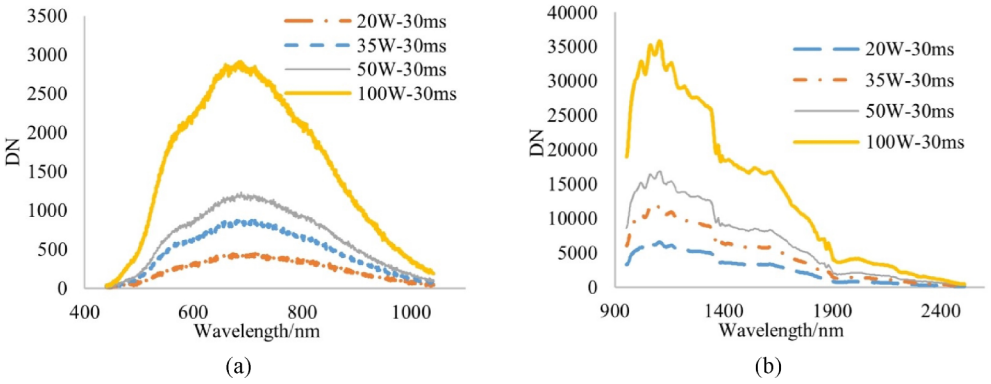

Fig. 10. Sensitivity test results for (a) the Headwall A-Series sensor and (b) the HySpex SWIR-384 sensor.

4.2. Radiation correction results

To validate the proposed radiation correction approach, experiments were conducted using the 37 strips of HeadWall VNIR and HySpex SWIR hyperspectral images. The position of the corresponding image points and the radiance contrast curves acquired by the HeadWall VNIR sensor are shown in Figs. 11 and 12. By comparing the radiance curves of adjacent strips with the same ground object before and after correction, it can be clearly seen that the radiation distortion between strips has been eliminated. The coefficient of determination R^2 for the sand, vegetation and soil before correction was 0.9221, 0.8948 and 0.7591, respectively, and the RMSE was 0.0045, 0.0047 and 0.0052, respectively. After the correction, the determination coefficient R^2 was improved to 0.9762, 0.9614 and 0.9347, respectively, and the RMSE was reduced to 0.0023, 0.0038 and 0.0027, respectively. The corresponding image points and the radiance contrast curves acquired by the HySpex SWIR sensor are shown in Figs. 13 and 14. The coefficient of determination R^2 for the sand, vegetation and soil before correction was 0.9921, 0.9871 and 0.9950, and the RMSE was 0.0013, 0.0023 and 0.0009. After the correction, the determination coefficient R^2 became 0.9981, 0.9987 and 0.9996, and the RMSE became 0.0006, 0.0006 and 0.0002.

The visual effect of the mosaicked image is the most intuitive way to judge the effect of radiation correction. However, due to the problems

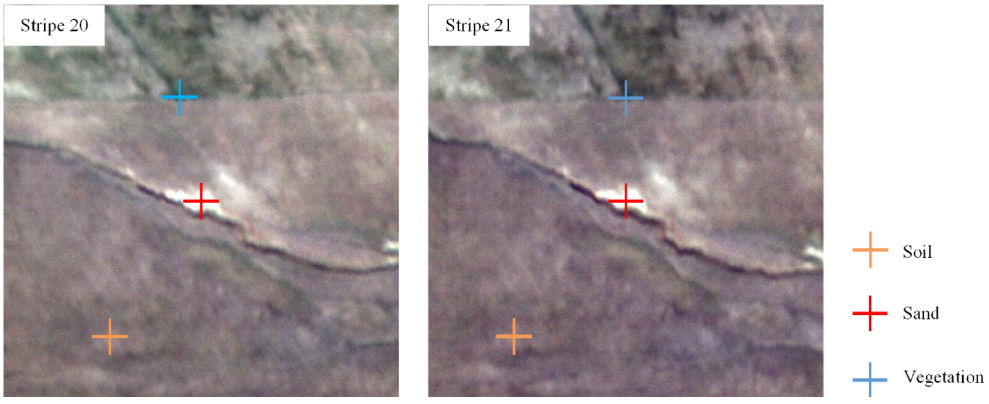

Fig. 11. The corresponding image points of adjacent strips acquired by HeadWall VNIR sensor.

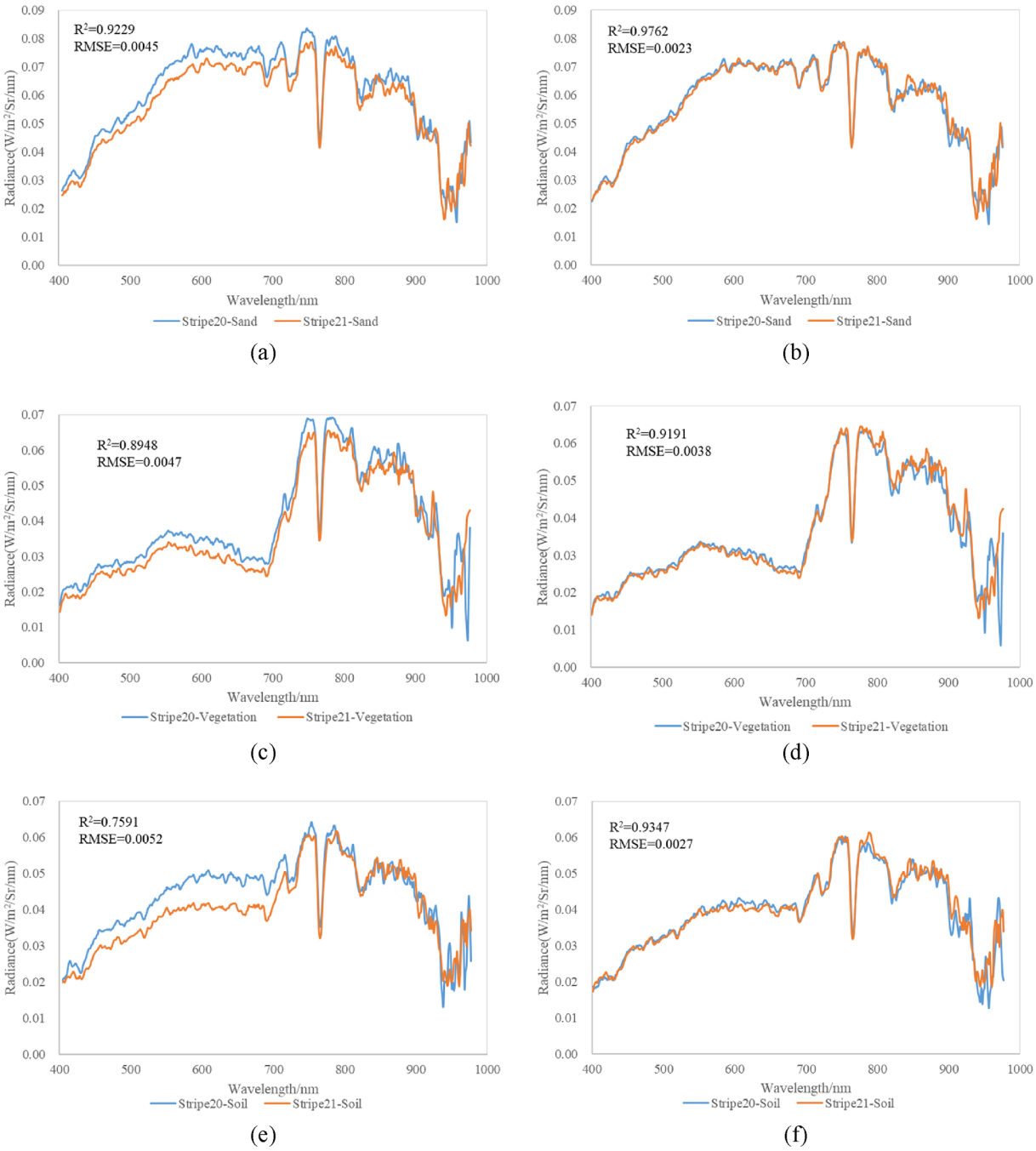

Fig. 12. HeadWall VNIR radiance comparison of corresponding image points before and after correction: (a), (c) and (e) are the radiance curves of sand, vegetation and soil before correction; (b), (d) and (f) are the radiance curves of sand, vegetation and soil after correction.

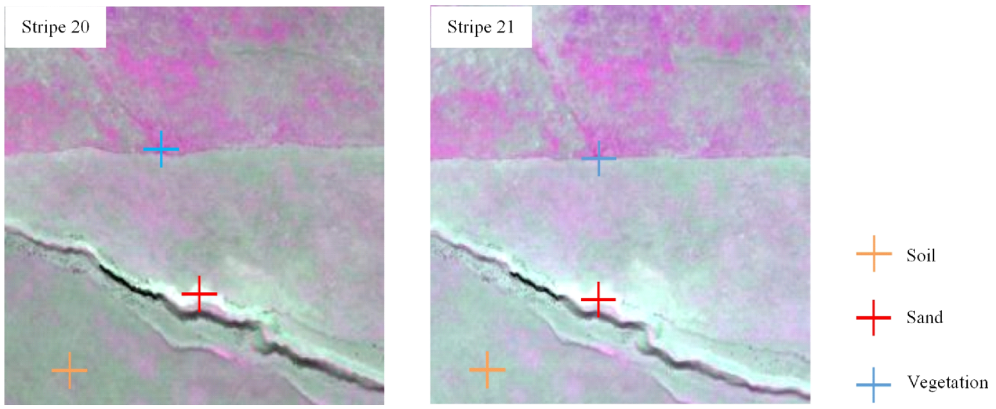

Fig. 13. The corresponding image points of adjacent strips acquired by HySpex SWIR sensor.

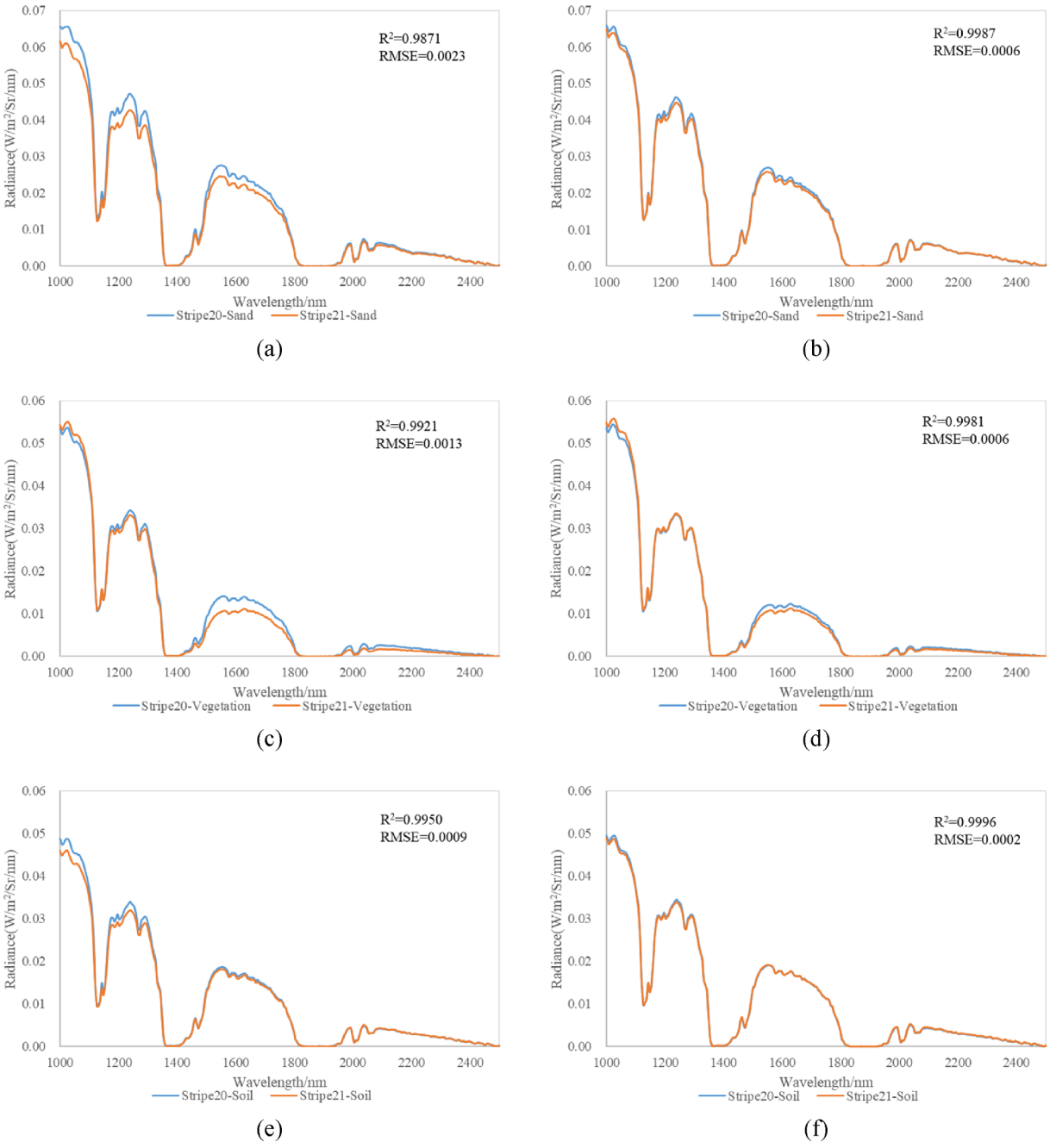

Fig. 14. HySpex SWIR radiance comparison of corresponding image points before and after correction: (a), (c) and (e) are the radiance curves of sand, vegetation and soil before correction; (b), (d) and (f) are the radiance curves of sand, vegetation and soil after correction.

of aircraft flight control and air route planning, the image acquired by HySpex SWIR sensor were lost in some areas. But it doesn't affect the correction results. The HeadWall VNIR and HySpex SWIR image mosaic result after radiation correction across strips without normalization of the exposure time is shown in Fig. 15(b) and Fig. 16(b). From the image, it can be seen that most of the distortion between strips has been eliminated, but the image is divided into several parts, which is caused by the inconsistency of the exposure time. Fig. 15(c) and Fig. 16(c) are the results after exposure time correction. We can see that the corrected image eliminates the brightness mismatch at the boundaries between the strips and achieves seamless mosaicking of all 37 strips.

4.3. Accuracy assessment

Here we selected two typical objects in one strip, vegetation and soil, for accuracy assessment. A comparison of the spectra is shown in Figs. 17 and 18. It can be seen that the positions of the peaks and troughs in the spectral curves of the ground objects are basically consistent with those of the ASD field spectroradiometer spectral curves. To further verify the atmospheric correction results, the image reflectance was compared with the measured ASD field spectroradiometer reflectance of vegetation. For the vegetation, the coefficient of determination R^2 for the Headwall VNIR imager and HySpex SWIR imager was

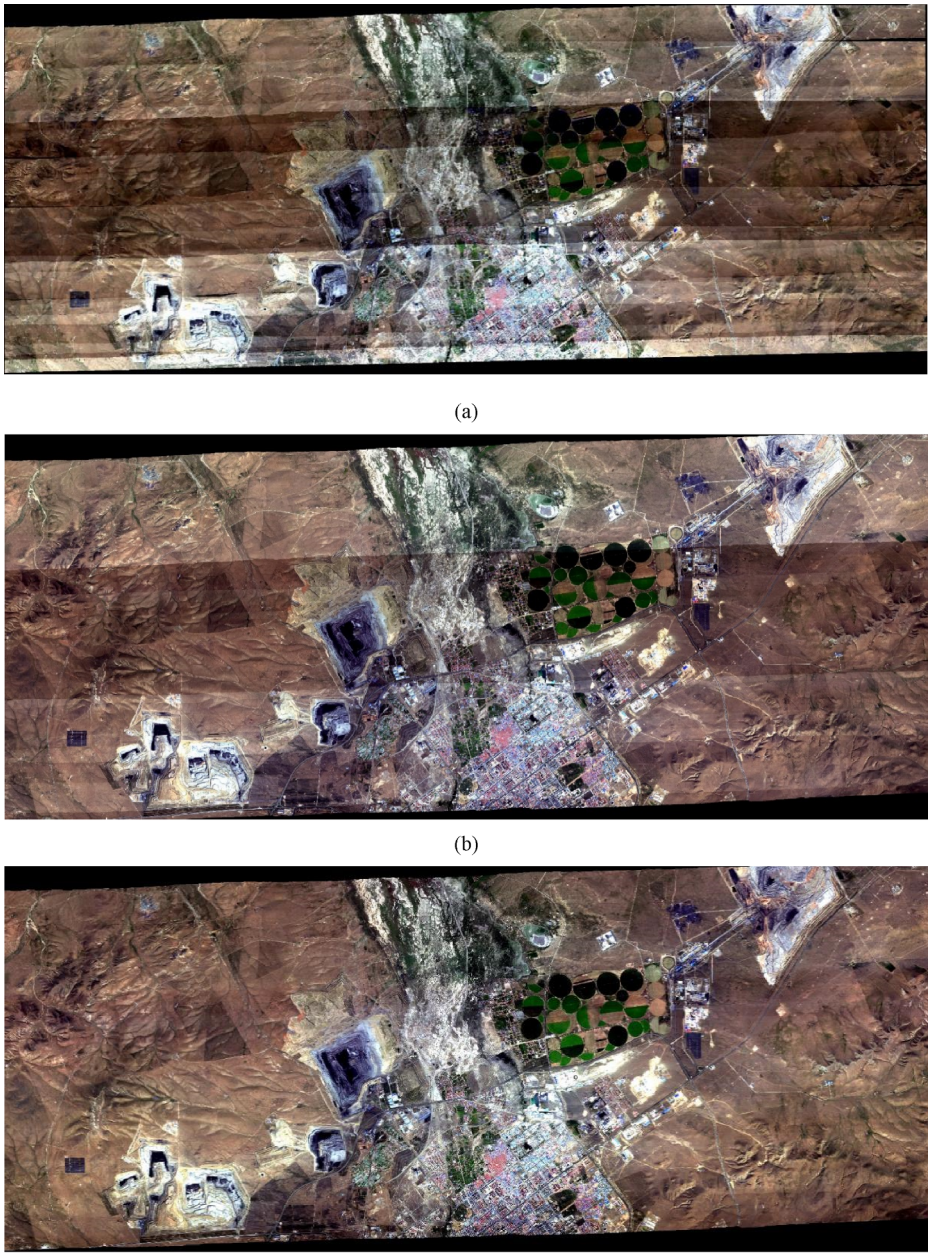

(a)

(b)

(c)

Fig. 15. The HeadWall VNIR results of the image mosaicking before and after correction. RGB color composition with band 161 (Wavelength:639.78 nm), band 101 (Wavelength:550.36 nm) and band 40 (Wavelength:459.45 nm). (a) Mosaic result before correction. (b) Mosaic result without exposure time correction. (c) Mosaic result after radiation correction.

0.9831 and 0.9345, the RMSE was 0.0120 and 0.0191, and the spectral angle was 3.096° and 4.662°, respectively. For the soil, the coefficient of determination R^2 for the Headwall VNIR imager and HySpex SWIR imager was 0.9757 and 0.7516, the RMSE was 0.0138 and 0.0716, and the spectral angle was 2.964° and 9.198°, respectively. The results show that the calibration results are reliable and can provide assurance for the qualitative and quantitative analysis of the follow-up work.

5. Discussion

In this study, we propose an advanced radiance correction method which considers the BRDF and radiation attenuation. This is useful for removing brightness gradient between adjacent strips and achieving seamless mosaicking of airborne hyperspectral images. Based on the results of the radiance comparison of corresponding image points before correction, the radiance difference is about 10% to 20%. We can see that, without correction, the errors of this magnitude will have a significant impact on quantitative analysis conducted thereafter. We suggest that this method should be taken as an important step in image processing when using airborne hyperspectral images for applications, such as biomass retrieval (Lu, 2006), water quality parameters estimation (Hakvoort et al., 2002) and soil heavy metals assessment (Tan

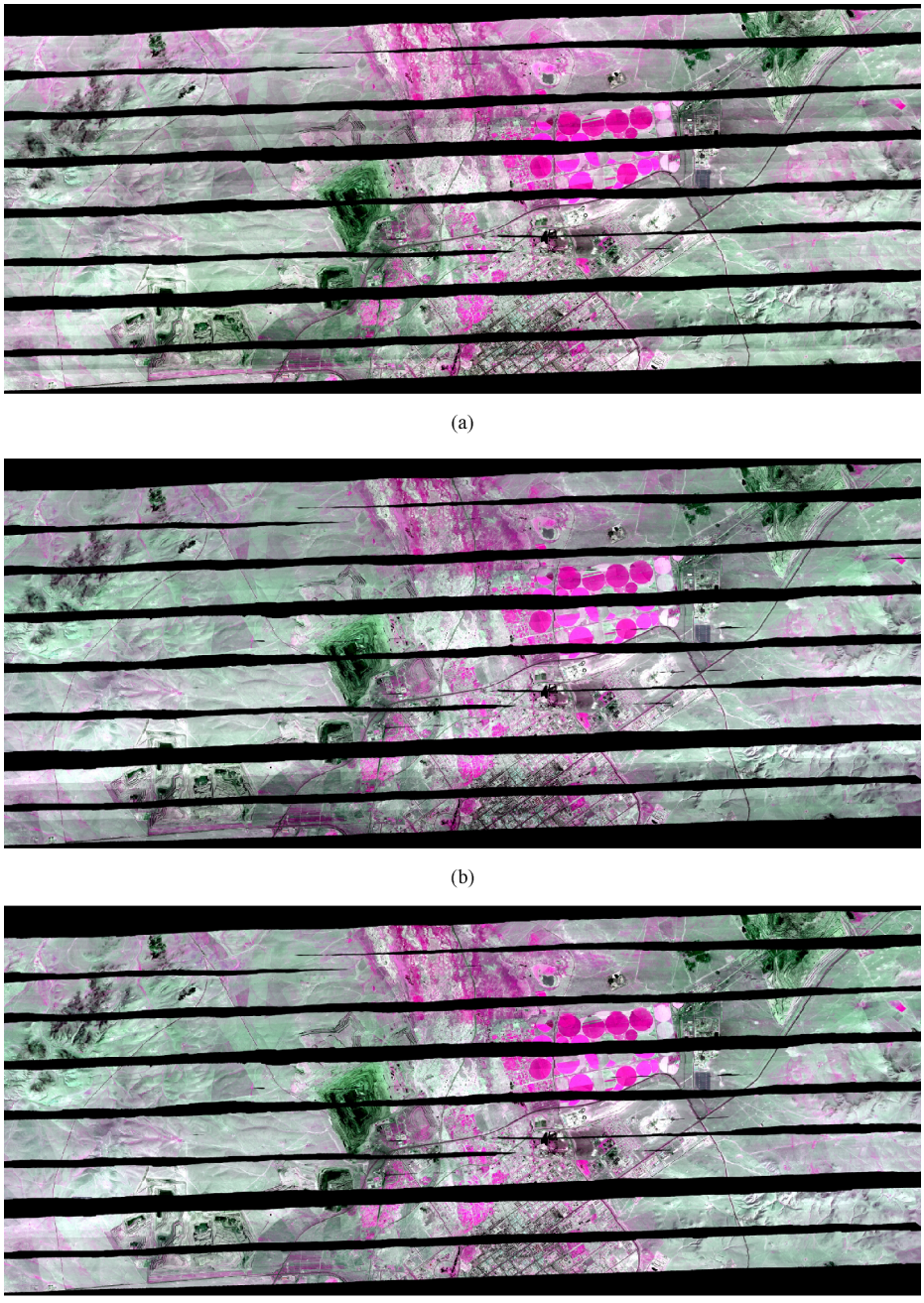

(a)

(b)

(c)

Fig. 16. The HySpex SWIR results of the image mosaicking before and after correction. RGB color composition with band 20 (Wavelength:1050.16 nm), band 117 (Wavelength:1581.36 nm) and band 57 (Wavelength:1255.87 nm). (a) Mosaic result before correction. (b) Mosaic result without exposure time correction. (c) Mosaic result after radiation correction.

et al., 2020), where accurate radiance measurements are critical. In these applications, the radiance measurements are used for modelling their relationship to the chemical parameters to retrieve and estimate. The BRDF effect and radiation attenuation will damage the true relationship and increase the model uncertainty, as a result the estimation will be inaccurate. For example, Honkavaara et al. (2013) compared the normalized root-mean-square-error (NRMSE) for biomass estimation before and after radiometrically correction, and found that using the radiometrically corrected data, the NRMSE was reduced by 6%. Feilhauer et al. (2010) introduced brightness normalization to the estimation of leaf chemistry, which increased the stability of the regression coefficients and improved the performance of regression model. Radiometric correction is mandatory in multitemporal data analysis for change detect. Paolini et al. (2006) found out change detection without data correction present more than 2 times higher than those obtained with corrected images.

While we focus on the correction of airborne hyperspectral images, it can be extended to the images from unmanned aircrafts (UAV). UAV's

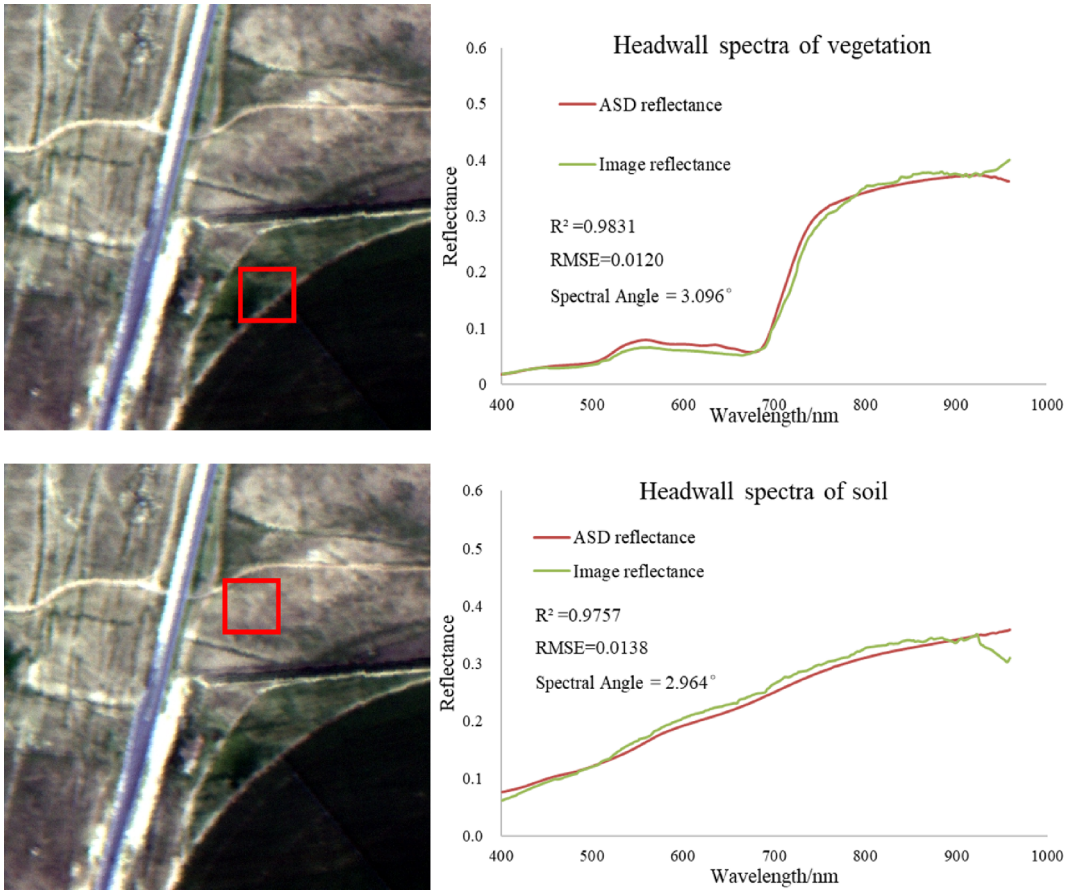

Fig. 17. Headwall VNIR spectral contrast diagram for vegetation and soil. RGB color composition using: band 161 (Wavelength:639.78 nm), band 101 (Wavelength:550.36 nm) and band 40 (Wavelength:459.45 nm).

flight stability is far less than that of manned aircraft, and the flight attitude changes dramatically. Therefore, the distortion caused by the radiation path difference is more obvious in the UAV hyperspectral images (Adão et al., 2017). The proposed radiation attenuation correction function considering the sensor attitude has potential in UAV hyperspectral images correction.

The proposed method is based on the assumption of radiation uniformity. It works well when the topographic relief is small and land-cover type is relatively single. The accuracy of this method will be reduced by large variations in terrain and land cover type. The hyperspectral sensor should be tested and calibrated in laboratory, including sensitivity test, spectral calibration and radiometric calibration to reduce the influence of these systematic errors, which add directly to the radiometric uncertainty for every spectrum in the image (Green, 1998). For example, the spectral shifts of 1 nm and bandwidths of 10 nm will result in a radiance error of up to 25% around water vapor absorption bands (Guanter et al., 2009). In addition, the use of high-precision positioning and orientation system will also improve the accuracy of this method.

6. Conclusion

In this paper, we have described BRDF and radiation attenuation correction for airborne hyperspectral imagery. Starting from the laboratory test, we completed wavelength calibration and radiation calibration. For the edge radiation distortion, we proposed a correction function combining the BRDF effect and radiation attenuation coefficients, and we normalized the exposure time, sun altitude angle, and sensor altitude angle according to the experimental design and actual situation of the flight. By comparing the radiance curves and the mosaicked image, it can be seen that this method achieves a good correction effect and can be effectively applied to hyperspectral data. Finally, we evaluated the radiation accuracy of the mosaicked image by comparing it with ASD field spectroradiometer ground spectral data. It was confirmed that the accuracy of the preprocessing results met the requirements of the subsequent applications.

The difference between the land-cover types was not obvious in this study area, so the image was not pre-classified and processed. Pre-classification of images before correction can reduce the impact of land-cover types, but it would increase the workload of the preprocessing. In the future, we will consider introducing the spectral correlation coefficient and Euclidean distance to screen the suitable pixels for constructing the fitting equation, so as to meet the requirements for multiple land-cover types in a study area.

Declaration of Competing Interest

The authors declare that they have no known competing financial interests or personal relationships that could have appeared to influence the work reported in this paper.

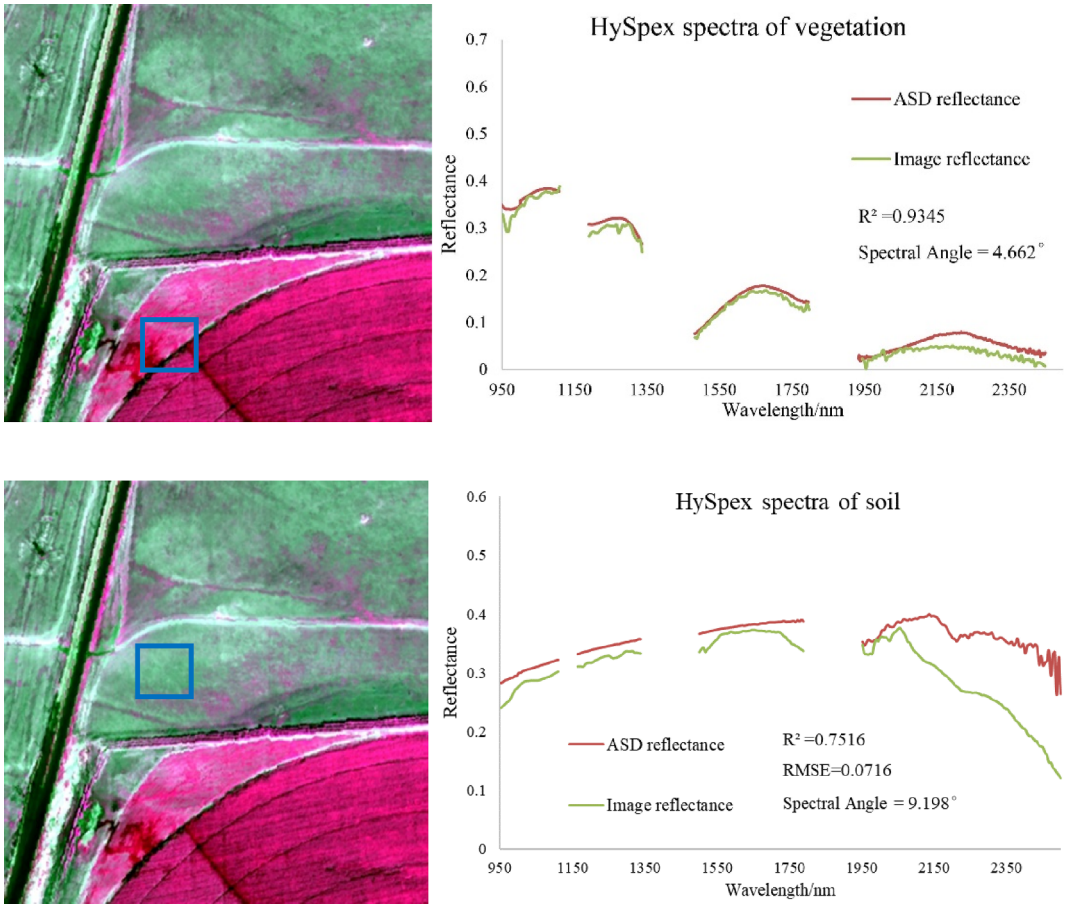

Fig. 18. HySpex SWIR spectral contrast diagram for vegetation and soil. RGB color composition using: band 20 (Wavelength:1050.16 nm), band 117 (Wavelength:1581.36 nm) and band 57 (Wavelength:1255.87 nm).

Acknowledgements

This research is supported in part by National Natural Science Foundation of China (No. 41871337), the National Key Research and Development Program of China (2016YFC0501107) and Priority Academic Program Development of Jiangsu Higher Education Institutions.

References

Adão, T., Hruška, J., Pádua, L., Bessa, J., Peres, E., Morais, R., Sousa, J.J., 2017. Hyperspectral imaging: A review on UAV-based sensors, data processing and applications for agriculture and forestry. Remote Sens. 9, 1110.

Baldocchi, D.D., Matt, D.R., Hutchison, B.A., Mcmillen, R.T., 1984. Solar radiation within an oak—hickory forest: an evaluation of the extinction coefficients for several radiation components during fully-leafed and leafless periods. Agric. For. Meteorol. 32, 307–322.

Berk, A., Bernstein, L.S., Robertson, D.C., 1987. MODTRAN: A moderate resolution model for LOWTRAN. Air Force Geophysics Laboratory Technical Report GL-TR-89-0122, Hanscom AFB, MA.

Brook, A., Ben-Dor, E., 2015. Supervised vicarious calibration (SVC) of multi-source hyperspectral remote-sensing data. Remote Sensing 7, 6196–6223.

Brook, A., Dor, E.B., 2011. Supervised vicarious calibration (SVC) of hyperspectral remote-sensing data. Remote Sens. Environ. 115, 1543–1555.

Brook, A., Polinova, M., Ben-Dor, E., 2018. Fine tuning of the SVC method for airborne hyperspectral sensors: the BRDF correction of the calibration nets targets. Remote Sens. Environ. 204, 861–871.

Chen, W., Yan, L., Li, Z., Jing, X., Duan, Y., Xiong, X., 2013. In-flight absolute calibration of an airborne wide-view multispectral imager using a reflectance-based method and its validation. Int. J. Remote Sens. 34, 1995–2005.

Choe, E., van der Meer, F., van Ruitenbeek, F., van der Werff, H., de Smeth, B., Kim, K.-W., 2008. Mapping of heavy metal pollution in stream sediments using combined geochemistry, field spectroscopy, and hyperspectral remote sensing: A case study of the Rodalquilar mining area, SE Spain. Remote Sens. Environ. 112, 3222–3233.

Cocks, T., Jenssen, R., Stewart, A., Wilson, I., Shields, T., 1998. The HyMapTM airborne hyperspectral sensor: the system, calibration and performance, Proceedings of the 1st EARSeL Workshop on Imaging Spectroscopy. EARSeL, pp. 37–42.

Colgan, M.S., Baldeck, C.A., Feret, J.B., Asner, G.P., 2012. Mapping savanna tree species at ecosystem scales using support vector machine classification and BRDF correction on airborne hyperspectral and LiDAR data. Remote Sens. 4, 3462–3480.

Collings, S., Caccetta, P., Campbell, N., Wu, X.L., 2010. Techniques for BRDF correction of hyperspectral mosaics. IEEE Trans. Geosci. Remote Sens. 48, 3733–3746.

Darvishzadeh, R., Skidmore, A., Schlerf, M., Atzberger, C., Corsi, F., Cho, M., 2008. LAI and chlorophyll estimation for a heterogeneous grassland using hyperspectral measurements. ISPRS J. Photogramm. Remote Sens. 63, 409–426.

Feilhauer, H., Asner, G.P., Martin, R.E., Schmidtlein, S., 2010. Brightness-normalized partial least squares regression for hyperspectral data. J. Quant. Spectrosc. Radiat. Transfer 111, 1947–1957.

Gege, P., Fries, J., Haschberger, P., Schötz, P., Schwarzer, H., Strobl, P., Suhr, B., Ulbrich, G., Vreeling, W.J., 2009. Calibration facility for airborne imaging spectrometers. ISPRS J. Photogramm. Remote Sens. 64, 387–397.

Green, R.O., 1998. Spectral calibration requirement for Earth-looking imaging spectrometers in the solar-reflected spectrum. Appl. Opt. 37, 683–690.

Guanter, L., Segl, K., Sang, B., Alonso, L., Kaufmann, H., Moreno, J., 2009. Scene-based spectral calibration assessment of high spectral resolution imaging spectrometers. Opt. Express 17, 11594–11606.

Hakvoort, H., De Haan, J., Jordans, R., Vos, R., Peters, S., Rijkeboer, M., 2002. Towards airborne remote sensing of water quality in The Netherlands-validation and error analysis. ISPRS J. Photogramm. Remote Sens. 57, 171–183.

Hapke, B., 2002. Bidirectional reflectance spectroscopy: 5. The coherent backscatter opposition effect and anisotropic scattering. Icarus 157, 523–534.

Hapke, B., 2012. Bidirectional reflectance spectroscopy 7: The single particle phase function hockey stick relation. Icarus 221, 1079–1083.

Honkavaara, E., Saari, H., Kaivosoja, J., Pölönen, I., Hakala, T., Litkey, P., Mäkynen, J., Pesonen, L., 2013. Processing and assessment of spectrometric, stereoscopic imagery collected using a lightweight UAV spectral camera for precision agriculture. Remote Sens. 5, 5006–5039.

Horvath, R., Braithwaite, J.G., Polcyn, F.C., 1970. Effects of atmospheric path on airbornemultispectral sensors. Remote Sens. Environ. 1, 203–215.

Jensen, D.J., Simard, M., Cavanaugh, K.C., Thompson, D.R., 2017. Imaging spectroscopy BRDF correction for mapping Louisiana's coastal ecosystems. IEEE Trans. Geosci. Remote Sens. 56, 1739–1748.

Kennedy, R.E., Cohen, W.B., Takao, G., 1998. Empirical methods to compensate for a view-angle-dependent brightness gradient in AVIRIS imagery. Remote Sens. Environ.

62, 277–291.
Lévesque, J., Staenz, K., 2004. A method for monitoring mine tailings revegetation using hyperspectral remote sensing, IGARSS 2004. 2004 IEEE International Geoscience and Remote Sensing Symposium. IEEE, pp. 575–578.
Li, F., Jupp, D.L., Thankappan, M., Lymburner, L., Mueller, N., Lewis, A., Held, A., 2012. A physics-based atmospheric and BRDF correction for Landsat data over mountainous terrain. Remote Sens. Environ. 124, 756–770.
Li, X., Strahler, A.H., 1992. Geometric-optical bidirectional reflectance modeling of the discrete crown vegetation canopy: effect of crown shape and mutual shadowing. IEEE Trans. Geosci. Remote Sens. 30, 276–292.
Lu, D., 2006. The potential and challenge of remote sensing-based biomass estimation. Int. J. Remote Sens. 27, 1297–1328.
Lucht, W., Schaaf, C.B., Strahler, A.H., 2000. An algorithm for the retrieval of albedo from space using semiempirical BRDF models. IEEE Trans. Geosci. Remote Sens. 38, 977–998.
Pan, C.-C., Yan, Q.-W., Ding, J.-W., Zhang, Q.-Q., Tan, K., 2018. Atmospheric correction of airborne hyperspectral image based on fruit fly-powell optimization algorithm. Spectroscopy Spectral Anal. 38, 224–234.
Paolini, L., Grings, F., Sobrino, J.A., Jiménez Muñoz, J.C., Karszenbaum, H., 2006. Radiometric correction effects in Landsat multi-date/multi-sensor change detection studies. Int. J. Remote Sens. 27, 685–704.
Patterson, E., Gillette, D., Stockton, B., 1977. Complex index of refraction between 300 and 700 nm for Saharan aerosols. J. Geophys. Res. 82, 3153–3160.
Polo, J., Ballestrín, J., Carra, E., 2016. Sensitivity study for modelling atmospheric attenuation of solar radiation with radiative transfer models and the impact in solar tower plant production. Sol. Energy 134, 219–227.
Rautiainen, M., Lang, M., Mottus, M., Kuusk, A., Nilson, T., Kuusk, J., Lükk, T.n., 2008. Multi-angular reflectance properties of a hemiboreal forest: An analysis using CHRIS PROBA data. Remote Sens. Environ. 112, 2627–2642.
Riaza, A., Buzzi, J., García-Meléndez, E., Carrère, V., Sarmiento, A., Müller, A., 2012. River acid mine drainage: sediment and water mapping through hyperspectral Hymap data. Int. J. Remote Sens. 33, 6163–6185.
Rogge, D., Bachmann, M., Rivard, B., Feng, J., 2012. Hyperspectral flight-line leveling and scattering correction for image mosaics. In: 2012 IEEE International Geoscience and Remote Sensing Symposium. IEEE, pp. 4094–4097.
Schaepman-Strub, G., Schaepman, M.E., Painter, T.H., Dangel, S., Martonchik, J.V., 2006. Reflectance quantities in optical remote sensing—Definitions and case studies. Remote Sens. Environ. 103, 27–42.
Schläpfer, D., Richter, R., Feingersh, T., 2014. Operational BRDF effects correction for wide-field-of-view optical scanners (BREFCOR). IEEE Trans. Geosci. Remote Sens. 53, 1855–1864.
Tan, K., Hu, J., Li, J., Du, P., 2015. A novel semi-supervised hyperspectral image classification approach based on spatial neighborhood information and classifier combination. ISPRS J. Photogramm. Remote Sens. 105, 19–29.
Tan, K., Wang, H., Chen, L., Du, Q., Du, P., Pan, C., 2020. Estimation of the spatial distribution of heavy metal in agricultural soils using airborne hyperspectral imaging and random forest. J. Hazard. Mater. 382 120987.
Tian, Y., Wu, W., Yang, G., 2016. Edge radiation distortion correction of whiskbroom airborne hyperspectral image by considering BRDF effect and atmospheric attenuation. J. Infrared Millimeter Waves 35, 701–707.
Van Stokkom, H.T.C., Guzzi, R., 1984. Atmospheric spectral attenuation of airborne remote-sensing data Comparison between experimental and theoretical approach. Int. J. Remote Sens. 5, 925–938.
Vermote, E.F., Tanré, D., Deuze, J.L., Herman, M., Morcette, J.-J., 1997. Second simulation of the satellite signal in the solar spectrum, 6S: An overview. IEEE Trans. Geosci. Remote Sens. 35, 675–686.
Wang, F., Gao, J., Zha, Y., 2018. Hyperspectral sensing of heavy metals in soil and vegetation: Feasibility and challenges. ISPRS J. Photogramm. Remote Sens. 136, 73–84.
Wang, X., Tan, K., Du, Q., Chen, Y., Du, P., 2019. Caps-TripleGAN: GAN-Assisted CapsNet for hyperspectral image classification. IEEE Trans. Geosci. Remote Sens. 57, 7232–7245.
Wu, Y., Besse, S., Li, J.-Y., Combe, J.-P., Wang, Z., Zhou, X., Wang, C., 2013. Photometric correction and in-flight calibration of Chang' E-1 Interference Imaging Spectrometer (IIM) data. Icarus 222, 283–295.
Wu, Y., Zhang, X., Liao, Q., Ji, J., 2011. Can contaminant elements in soils be assessed by remote sensing technology: a case study with simulated data. Soil Sci. 176, 196–205.
Yu, J., Yan, B., Liu, W., Li, Y., He, P., 2017. Seamless mosaicking of multi-strip airborne hyperspectral images based on hapke model. In: International Conference on Sensing and Imaging. Springer, pp. 285–292.